Role of defects in carbon materials during metal-free formic acid dehydrogenation†

Ilaria Barlocco,[a] Sofia Capelli,[a] Xiuyuan Lu,[b] Simone Tumiati,[c] Nikolaos Dimitratos,[d] Alberto Roldan [iD] *[b] and Alberto Villa [iD] *[a]

Commercial graphite (GP), graphite oxide (GO), and two carbon nanofibers (CNF-PR24-PS and CNF-PR24-LHT) were used as catalysts for the metal-free dehydrogenation reaction of formic acid (FA) in the liquid phase. Raman and XPS spectroscopy demonstrated that the activity is directly correlated with the defectiveness of the carbon material (GO > CNF-PR24-PS > CNF-PR24-LHT > GP). Strong de-activation phenomena were observed for all the catalysts after 5 minutes of reaction. Density functional theory (DFT) calculations demonstrated that the single vacancies present on the graphitic layers are the only active sites for FA dehydrogenation, while other defects, such as double vacancies and Stone–Wales (SW) defects, rarely adsorb FA molecules. Two different reaction pathways were found, one passing through a carboxyl species and the other through a hydroxymethylene intermediate. In both mechanisms, the active sites were poisoned by an intermediate species such as CO and atomic hydrogen, explaining the catalyst deactivation observed in the experimental results.

1. Introduction

The increasing demand for fossil fuels and the alarm related to global warming are turning the attention of both academia and industry to use sustainable energy sources. Amongst them, hydrogen is becoming one of the most promising alternatives.[1,2] The versatility of hydrogen lies in the possibility to convert it to electricity or heat through electrochemical and catalytic processes. To achieve this goal, noble metal based cat-alysts have been employed in different hydrogen production reactions because of their good activity, selectivity and stability.[3–11] However, the use of noble metals raises doubts about the overall sustainability of the process, hence, pointing towards the use of alternative metal free analogues.[12–14] Carbon-based catalysts are attracting significant attention to reduce the use of metals in heterogeneous catalytic reactions. Carbocatalysis in gas phase reactions has been investigated in detail for the dehydrogenation of alkenes and alkanes.[15–17] It has also been effectively applied in electrocatalytic[18] and

photocatalytic processes.[19] The stability of carbocatalysts in liquid phase reactions makes them successful catalysts in different kinds of reactions such as oxidation of alcohols[20,21] and benzene,[22] reductions (such as acetylene, carbon–carbon multiple bonds and functionalized benzenes),[23,24] and coup-ling reactions (e.g. aldol condensation and oxidative coupling of amines).[25,26]

Indeed, carbon materials have the advantage of being easily tuned through variation in their structure, for example, chan-ging the surface area and porosity and adding functional groups or generating topological defects.[27–29] The introduction of heteroatoms (e.g. O, N, P and B)[30] into the carbon honey-comb lattice induces changes in the electronic properties of the material making these doped metal-free catalysts very suc-cessful employed, for example in oxidation reactions.[31,32] Combining intrinsic topological defects (i.e. vacancies and non-hexagonal rings derived from lattice reconstruction) and the presence (or absence) of heteroatoms leads to a huge number of tuning possibilities to influence the carbocatalyst's activity.[33–36] Qiu et al. reported that the activity of different activated carbons in acetylene hydrochlorination is correlated with the amount of carbon defects.[37] Moreover, Gao et al. have shown that the introduction of nitrogen into graphite can enhance the chemical reactivity of the carbon atoms activating molecular oxygen and hydrocarbons at room temperature.[38] Jia et al. demonstrated how defects obtained by removing heteroatoms are important for the oxygen reduction reaction (ORR), oxygen evolution reaction (OER), and hydrogen evol-ution reaction (HER).[39]

[a]Dipartimento di Chimica, Università degli Studi di Milano, via Golgi 19, I-20133 Milano, Italy. E-mail: Alberto.Villa@unimi.it

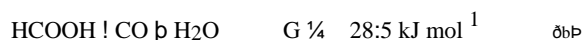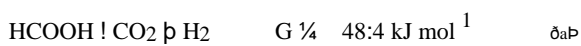[b]Cardiff Catalysis Institute, School of Chemistry, Cardiff University, Main Building, Park Place, CF10 3AT Cardiff, UK. E-mail: RoldanMartinezA@cardiff.ac.uk

[c]Dipartimento di Scienze della Terra Ardito Desio, Università degli Studi di Milano, via Botticelli 23, I-20133 Milano, Italy

[d]Dipartimento di Chimica Industriale e dei Materiali, Alma Mater Studiorum Università di Bologna, Viale Risorgimento 4, 40136 Bologna, Italy

†

In the present work, we studied the role of the defects in four different commercial carbon materials, i.e. graphite, graphite oxide, and two carbon nanofibers with different gra-phitization degrees (PR24-PS and PR24-LHT), by investigating the formic acid (FA) dehydrogenation reaction in the liquid phase under mild reaction conditions. FA was selected as the substrate because it is one of the most suitable and environ-mentally friendly chemicals for the storage and production of H_2.[40] FA is a good candidate for hydrogen storage (4.4 wt%) and for recycling CO_2.[41,42] FA is a non-toxic compound obtained from the catalytic conversion of biomass (i.e. hydration of 5-HMF found in lignocellulose[43,44]) and it can be easily decomposed using homogeneous and heterogeneous catalysts through two possible pathways:

$$HCOOH \rightarrow CO_2 + H_2 \qquad G = 48.4 \text{ kJ mol}^{-1} \qquad (a)$$

$$HCOOH \rightarrow CO + H_2O \qquad G = 28.5 \text{ kJ mol}^{-1} \qquad (b)$$

The desired dehydrogenation reaction (a) produces H_2 and CO_2, whereas dehydration (b) produces CO and H_2O, which needs to be avoided, i.e. carbon monoxide concentration should remain below 20 ppm in order to obtain ultrapure hydrogen for application in fuel cells.[45] To understand the role of graphite defects in these reactions, we carried out a systema-tic investigation combining experiments and computational simulations on the FA adsorption and decomposition mecha-nisms on different graphitic structures to reveal the role of topological defects present in the carbocatalysts.

2. Experimental and computational methods

2.1 Materials and chemicals

CNFs PR24-PS and PR24-LHT were obtained from the Applied Science Company. The as-grown nanofibers underwent post-treatment at various temperatures to remove the polyaromatic carbon layer covering their outer surface. The thermal treat-ments were carried out at 700 and 1500 °C for PR24-PS and PR24-LHT, respectively. Graphite was purchased from Johnson Matthey. Graphite oxide was bought from the Sixth Element Company (Changzhou, China). Formic acid (≥95%) was pur-chased from Sigma-Aldrich and deionised water was used as the reaction solvent.

2.2 Formic acid decomposition

Liquid-phase FA decomposition was carried out in a 100 mL two-neck round-bottom flask placed in a water/ethylene glycol bath with a magnetic stirrer and a reflux condenser.

Typically, 10 mL of an aqueous solution of 0.5 M HCOOH was placed in the reactor and heated at a constant reaction temperature of 80 °C. Once the solution reached the desired temperature, the required amount of catalyst (formic acid/cata-lyst weight ratio of 10/1) was added and the solution was stirred using a magnetic stirrer.

2.3 Product analysis

Formic acid conversion was analysed using high-performance liquid chromatography (HPLC). The conversion was calculated according to the equation $mol_{in} - mol_{out}/(mol_{in} \times 100)$, where mol_{in} and mol_{out} are the initial and the remaining moles, respectively. H^+ chromatographic column was used (Alltech OA-10 308, 300 mm_7.8 mm) with a UV detector set at 210 nm. Liquid samples were withdrawn periodically (200 μL) and diluted to 5 mL with H_3PO_4 solution (0.1 wt%), which was also the eluent of the analysis. The isocratic eluent flow was set at 0.4 ml min^{-1}. Analysis of the gas was performed using an online micro-gas chromatograph (Agilent 3000A) every 7 min. This instrument is equipped with a TCD detector and two different columns: (a) a molecular sieve module and (b) an OV-1 module (stationary phase of polydimethylsiloxilane). Gases (CO and CO_2) were quantified using calibration curves created from commercial standards.

2.4 Catalyst characterization

Carbon samples were characterized by X-ray photoelectron spectroscopy (XPS), BET, ICP-OES and Raman spectroscopy. Thermo Scientific K-alpha+ spectrometer was used for XPS measurements. The samples were analysed using a monochro-matic Al X-ray source operating at 72 W, with the signal aver-aged over an oval-shape area of 600×400 μ. Data were recorded at 150 eV for survey scans and 40 eV for high resolu-tion (HR) scans with a 1 eV and 0.1 eV step size, respectively. CASAXPS (v2.3.17 PR1.1) was used for the analysis of the data, using Scofield sensitivity factors and an energy exponent of −0.6.

Raman spectroscopy was performed using a Horiba LabRam HR Evolution micro-Raman spectrometer equipped with a green solid-state laser (532 nm) focused through a 100× objective, giving a spatial resolution of approximately 1 μm. The micro-Raman system was set with 300 lines per mm grating; the spectrum was collected with a final laser power of about 0.1 mW at the sample surface measured through a hand-held power meter. Spectra were calibrated using the 520.7 cm^{-1} line of a silicon wafer. The sample was scanned at an attenuation time of 300 s and 2 scans were carried out to give a spectrum.

Quantachrome Autosorb was used to measure the surface area and pore size. The samples were degassed at 120 °C for 3 h before starting the measurements. All the surface areas were evaluated using the Brunauer–Emmett–Teller (BET) method.

The presence of possible residual metal was analyzed by inductively coupled plasma optical emission spectroscopy (ICP-OES) using a PerkinElmer Optima 8000 emission spectrometer.

2.5 Computational method

Periodic plane-wave density functional theory (DFT) calcu-lations were performed using the Vienna ab initio simulation package (VASP).[46,47] We employed generalised gradient approximation by Perdew–Burke–Ernzerhof functional revised

for solids[48] and a kinetic energy of 450 eV to expand the plane-waves of the Kohn–Sham valence states.[49] All the calculations include the long-range dispersion correction approach by Grimme,[50,51] which is an improvement on pure DFT to evalu-ate molecular interactions.[52–55] We also included the implicit solvation model as implemented in VASPsol describing the bulk water effect of electrostatics, cavitation, and dispersion on the FA interaction with the C-materials.[56,57] The optimiz-ation thresholds were 10^{-5} eV and 0.01 eV Å^{-1} for electronic and ionic force relaxation, respectively. The Brillouin zone was sampled by a Γ-centre k-point mesh generated through a Monkhorst–Pack grid of $5 \times 5 \times 1$ k-points, which ensures no Pulay stress.[58] In order to improve the convergence of the Brillouin-zone integrations, the partial occupancies were deter-mined using the first order Methfessel–Paxton method correc-tions smearing with a set width for all calculations of 0.1 eV.

Carbon materials were represented by a single layer slab model of a 6×6 pristine supercell containing different defects: single vacancy (SV), double vacancy (DV) and three different Stone–Wales defects (SW1, SW2 and SW3). The supercell was in a hexagonal lattice with the unit cell vectors a and b in the surface plane and c perpendicular to the graphene plane; a and b were optimized at 14.8199 Å. We added a vacuum width of 15 Å (c), which is large enough to avoid spurious periodic interactions.

In order to compare the formation energy of the defective surfaces with the energy of pristine graphene, we describe the difference in energy (E) as

$$E ¼ E_S \quad n \quad E_C; \qquad (1)$$

where E_S is the energy of the considered surface, n the number of atoms in it, and E_C is the energy of the single carbon atom in the hexagonal lattices of graphene. We defined the adsorption energy (E_{ADS}) as the difference between the combined system and the isolated species, while the reaction energy (E_R) of each step was calculated as the total energy difference between the final state (product(s)) and the initial state (reactant(s)).

3. Results and discussion

We pre-treated the carbocatalysts with a solution of 0.1 M HCl to remove possible impurities and confirmed the absence of metal impurities using ICP-OES. We measured the initial cata-lytic activity after 5 minutes of reaction (Table 1) and we observed that the most active catalysts were GO and PR24-PS with a FA conversion of 28.5 and 27.5%, respectively, followed by PR24-LHT (13.9%) and GP (3%). However, beyond the 5 minutes of reaction, all the catalysts suffered a strong de-activation (Fig. 1). Analysis of the gases evolved revealed that the reaction mainly follows the dehydrogenation pathway with a selectivity of 70–75% to $H_2 + CO_2$ and 25–30% to $CO + H_2O$ for all systems.[59]

To identify the active sites of these catalysts and rationalize their deactivation, we characterized their structure and surface properties using BET, Raman spectroscopy and XPS. Graphite

Table 1 Characteristics of the carbon catalyst derived from BET, Raman and XPS analyses and their initial (5 minutes of reaction) catalytic activity towards FA decomposition

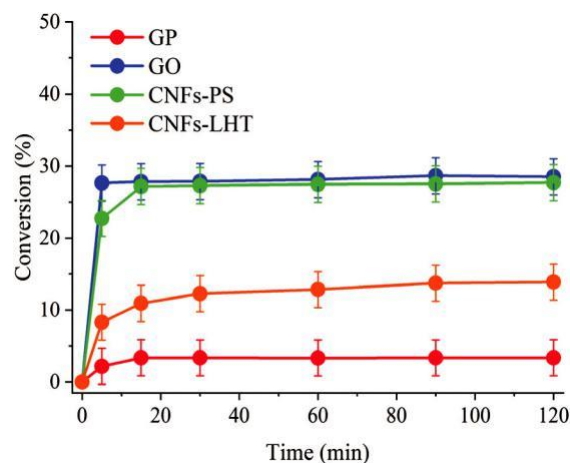| Catalyst	Surface area ($m^2 g^{-1}$)	Raman I_D/I_G	XPS sp^2/sp^3	O/C	Conversion (%)
GP	14	0.09	—	0.02	3.0
PR24-PS	43	1.54	4.00	0.13	27.5
PR24-LHT	38	0.60	7.00	0.09	13.9
GO	12	1.64	0.03	0.45	28.5

Fig. 1 Conversion trend for the formic acid decomposition reaction for the different carbonaceous materials: graphite (GP), graphite oxide (GO) and CNFs PR24-PS and PR24-LHT. To ensure reproducibility, the experi-ments were repeated three times (experimental error ± 2.5%).

and graphite oxides show a surface area of 14 and 12 $m^2 g^{-1}$, respectively, whereas PR24-PS and PR24-LHT presented a higher surface area (43 and 38 $m^2 g^{-1}$, respectively) (Table 1). Raman spectroscopy was used to investigate the graphitization degree of carbon materials. Raman spectra show two bands at around 1600 cm^{-1} (G band) and 1350 cm^{-1} (D band) which are characteristic carbonaceous materials.[60] The G band is gener-ated by the CνC stretching vibrations in the graphite lattice and it is related to structurally ordered graphite domains.[60] The D band corresponds to the A^1_g mode, which is forbidden according to the selection rules in graphite, but it is activated in the presence of structural defects or in plane substitutional heteroatoms.[60] Hence, we used the ratio of the integral intensi-ties of D and G bands (I_D/I_G) as an index of the defectiveness of the graphite layers (Table 1). All carbon materials studied in this work present both D and G Raman bands (Fig. S1†) with the following I_D/I_G ratio: GO (1.64) > PR24-PS (1.54) > PR24-LHT (0.60) > GP (0.09). It should be noted that CNFs ID/IG ratio decreased (1.54 and 0.60 for PR24-PS and PR24-LHT, respectively), increasing the annealing temperature (700 °C and 1500 °C for PR24-PS and PR24-LHT, respectively).

We employed XPS to record the survey and the high-resolu-tion (HR) spectra of C 1s species. Survey spectra revealed the presence of both C and O elements, while no N or S was

detected. From HR C 1s spectra, an evaluation of the relative concentration of C–C sp^3 and C=C sp^2 species in the different materials was performed (Table S1 and Fig. S2†). The component at approximately 284.4 eV can be attributed to the presence of sp^2-hybridised carbon species, whereas the one at 285 eV indicates the presence of sp^3-hybridized carbon species.[61] XPS-HR C 1s spectra confirmed a high graphitization degree in the case of GP, where carbon is mainly present in the sp^2 form, whereas a combination of sp^2 and sp^3 is present for the other carbonaceous materials with a sp^2/sp^3 ratio of 7.00, 4.00 and 0.03 for PR24-LHT, PR24-PS and GO, respectively (Table 1). XPS survey analysis revealed a higher oxygen content for GO (O/C of 0.45), while the carbon nanofibers showed an O/C ratio of about 0.1. In contrast, GP contained a very low amount of oxygen, as expected for highly graphitized materials (Table 1). The deconvolution of the O 1s signal identified four main oxygen groups and the peak assignment has been made following the literature:[62] (i) O–(C=O*)–$C_{aliphatic}$ at a binding energy (E$_B$) of 532 eV, (ii) O–C–O/C–O–C at E$_B$ = 533 eV, (iii) O*–(C=O)–$C_{aliphatic}$ at E$_B$ = 534 eV and (iv) H$_2$O at BE = 537 eV (Table S1 and Fig. S3†). Oxygen is mainly presented in the form of O–(C=O*)–$C_{aliphatic}$ on the surface of GP, PR24-PS and PR24-LHT (92%, 75.20% and 74.12%, respectively), and in the form of O–C–O/C–O–C (77.29%) in the GO sample (Table S1†).

We plotted the FA conversion as a function of the I_D/I_G ratio, the O/C ratio, and the different oxygen groups to identify their relationship and rationalize the activity of the carbon materials with their defectiveness and the presence of oxygen functional groups (Fig. 2). We found a linear relationship between the FA conversion and the I_D/I_G ratio (R^2 = 0.99), whereas there is no direct correlation of the activity with the oxygen groups present on the surface (Fig. S4†).
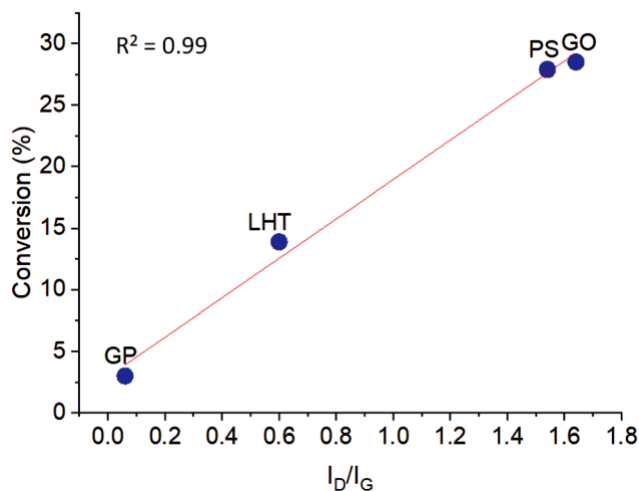

Fig. 2 Linear correlation of conversion vs. I_D/I_G. PS: pyrolytically stripped carbon nanofibers, LHT: carbon nanofibers heat-treated to 1500 °C, HHT: carbon nanofibers heat-treated up to 3000 °C, GP: pristine graphene, GO: graphene oxide.

3.1 DFT study

3.1.1 Graphitic structures. The correlation between the previous characterization results and the FA decomposition activity suggests that the defects on the graphitic matrix participate in the mechanism for the activation of formic acid, such as vacancies and Stone–Wales defects rather than the oxygen groups as previously suggested by Raman and conversion correlations. We performed a systematic computer simulations study based on density functional theory to shed light on the FA decomposition and catalyst deactivation mechanisms.

Six different graphitic surfaces were modeled according to the reported defects in the literature[63] (Fig. 3): pristine graphite, Single Vacancy (SV), Double Vacancy (DV) and three different Stone–Wales defects (SW1, SW2 and SW3).

SV and DV were prepared by removing, respectively, one and two neighboring carbon atoms from pristine graphene and re-optimizing the structure at fixed supercell lattice. Similarly, SW1 was found rotating a C–C bond of 90° from pristine graphene, while SW2 was obtained rotating a bond of 90° from DV, and SW3 rotating a second different bond of 90° from SW2.[64] The flexibility of the honeycomb lattice allows its reconstruction to minimize dangling bonds, thus providing further stability, e.g. forming non-hexagonal rings. In the DV defect, the optimization leads to an octagon and two pentagons. SW1 is a point defect where four hexagons (without C-vacancies) are transformed into two pentagons and two heptagons. The octagon present in the DV structure transforms it into the SW2 surface composed of three pentagons and three heptagons, while SW3 contains four pentagons, one hexagon and four heptagons. The presence of these defects forces the rearrangement of the C electronic structure, which also influences the catalytic properties and the stability of the material. All the surfaces show a positive relative energy, meaning that they are less thermodynamically favorable than pristine graphene (Table 2). In agreement with previous experiments, our result confirms that the formation energies of SV and DV are near 7.5 eV (ref. 65 and 66), while the one of SW1 is around 5 eV (ref. 67 and 68) compared to pristine graphene. SW2 and SW3 are more stable than DV as an even number of missing carbon atoms permits a full reconstruction of the bonds decreasing the dangling bonds,[69] which also agrees with the study by Do Lee et al.[70] In agreement with our results, it has also been reported that the reconstruction energy of DV forming SW2 is about 1 eV lower than the one of DV, and that the energy of SW3 lies between the two energies of DV and SW2.[65,66]

3.1.2 FA adsorption. We brought formic acid to non-equivalent surface sites with different molecular orientations and relaxed the structure leading to different adsorption modes. We selected the most stable adsorption configurations of each surface to perform the subsequent FA decomposition reaction steps (Fig. 4).

In accordance with previous studies, pristine graphene has an inactive π-conjugation, which is not sensitive in the adsorp-
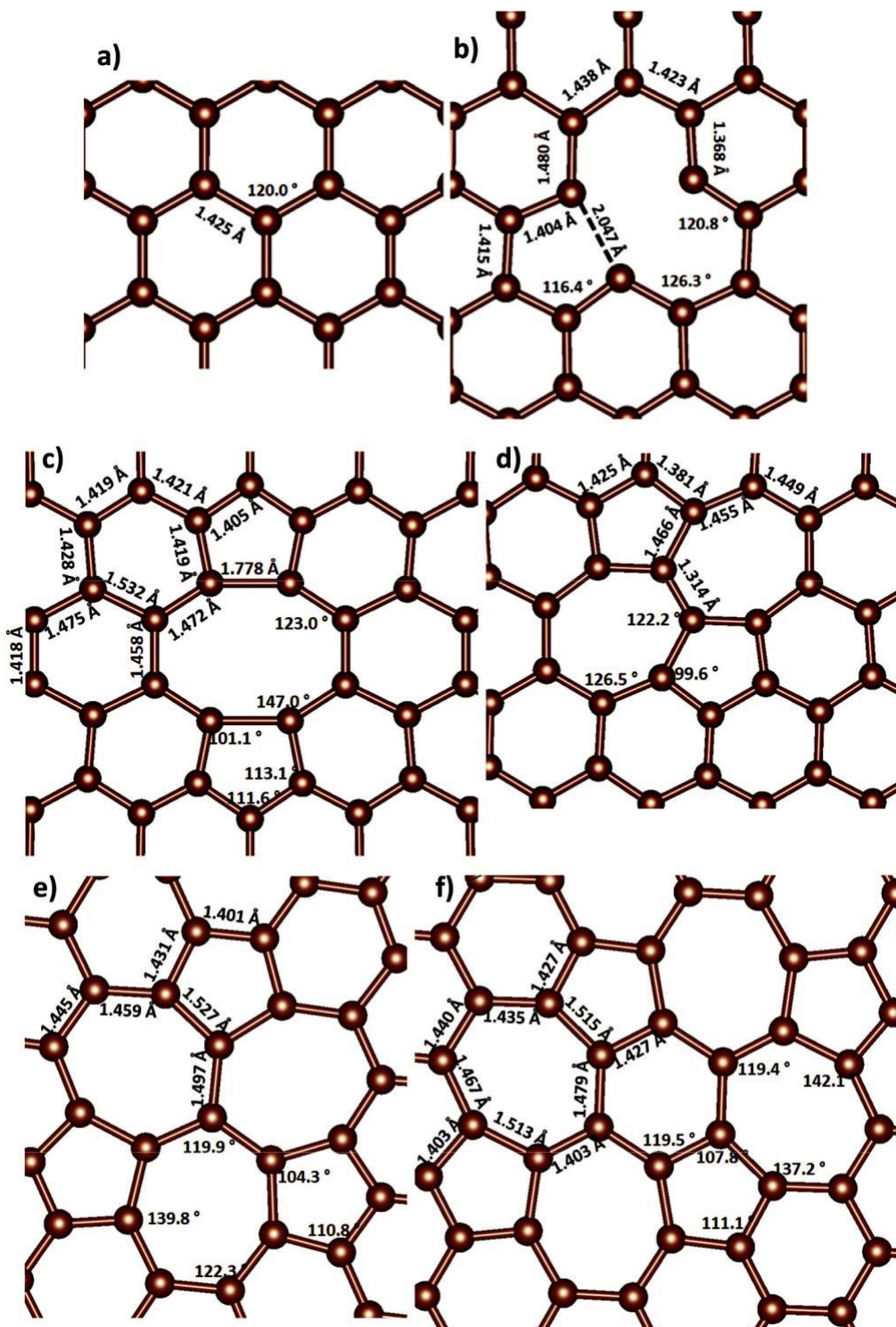
Fig. 3 Top view of the optimized graphitic surfaces: (a) pristine graphene, (b) SV, (c) DV, (d) SW1, (e) SW2 and (f) SW3. Inset shows the distances (Å) and angles (°) of interest. Carbon atoms are represented in brown.

tion of molecules.[71–73] In fact, the pristine graphene is not capable to chemically bind molecular formic acid on its surface. Another possible way to adsorb FA is through dissocia-tive adsorption (DA), i.e. where the bond between H and C (or O) breaks forming a new bond with the surface. This pathway

was shown by Solymosi when FA adsorbs on the Pt-based cata-lyst forming the formate species.[74] Nevertheless, graphene remains incapable to adsorb the dissociated FA.

Wang et al. demonstrated that by increasing the amount of defects in the graphene surface, the activity towards the acti-

Table 2 Relative energies of the different graphitic surfaces

Surface	E (eV)
Graphene (G)	0.00
Single vacancy (SV)	+7.22
Double vacancy (DV)	+7.17
Stone−Wales defect (SW1)	+4.89
Stone−Wales defect (SW2)	+5.71
Stone−Wales defect (SW3)	+6.70

vation of peroxymonosulfate is enhanced due to the uncon-fined π-electrons.[75] We summarize the adsorption energies (E_{ADS}) on the defective structures in Table 3 and it is seen that only SV and DV have a favorable (exothermic) interaction with FA.

The molecular adsorption of FA on SV and DV slightly dis-torts the graphitic structure: the distance between two carbon atoms increases to 0.676 Å and 1.051 Å, respectively (Fig. 3a and b). Indeed, it has been demonstrated that SV defect has great affinity with different functional groups, e.g. CO^{76} and O in peroxymonosulfate leading to the O−O cleavage.[75] Xu et al. proved that DV is also reactive (compared with pristine gra-phene) upon its exposure to different DNA bases.[77] In contrast, the SW surfaces showed only FA physisorption. We then con-sidered the dissociative adsorption pathway on SW structures and found that SW1 is the only SW structure able to provide an exothermic adsorption site upon C−H bond scission (Fig. 5). Instead, SW2 and SW3 showed endothermic adsorp-tions (Table 3). The dissociative adsorption of FA on SV and DV surfaces was also considered. On the first surface, it leads to one stable structure where COOH and H are adsorbed on the surface giving a reaction energy of −3.42 eV (Fig. S5†), which can be considered as the subsequent dehydrogenation step in the reaction pathway. In contrast, for the DV system, the structure obtained gave an endothermic E_B of +0.20 eV denoting this pathway unlikely.

To confirm that the activity does not depend on the oxygen groups present on the carbon surface, different types of oxygen functionalities on pristine graphene were optimized in accord-ance with the XPS analysis (Table S1†). We evaluated epoxides, hydroxyl and oxygen incorporated into the graphene structure (Fig. S5†), but we did not find any exothermic adsorption of FA, demonstrating that these types of functionalities are not active for the FA decomposition reaction.

3.1.3 FA decomposition. The decomposition of molecularly adsorbed FA on SV and DV was studied considering both dehy-drogenation and dehydration reaction pathways leading to car-boxyl (COOH*) and formate (HCOO*) intermediates, respect-ively.[7] Thus, we proceeded by considering the C−H bond scis-sion and comparing its reaction energy with the one for O−H bond scission on SV and DV surfaces.

Single vacancy (SV) system. The dissociation of the C−H bond leads to co-adsorption of COOH and H (Fig. S6†), which are stabilised by the SV structure giving a reaction energy (E_R) of −0.71 eV. While the co-adsorbed hydrogen was considered to migrate across the graphitic structure, the following reaction
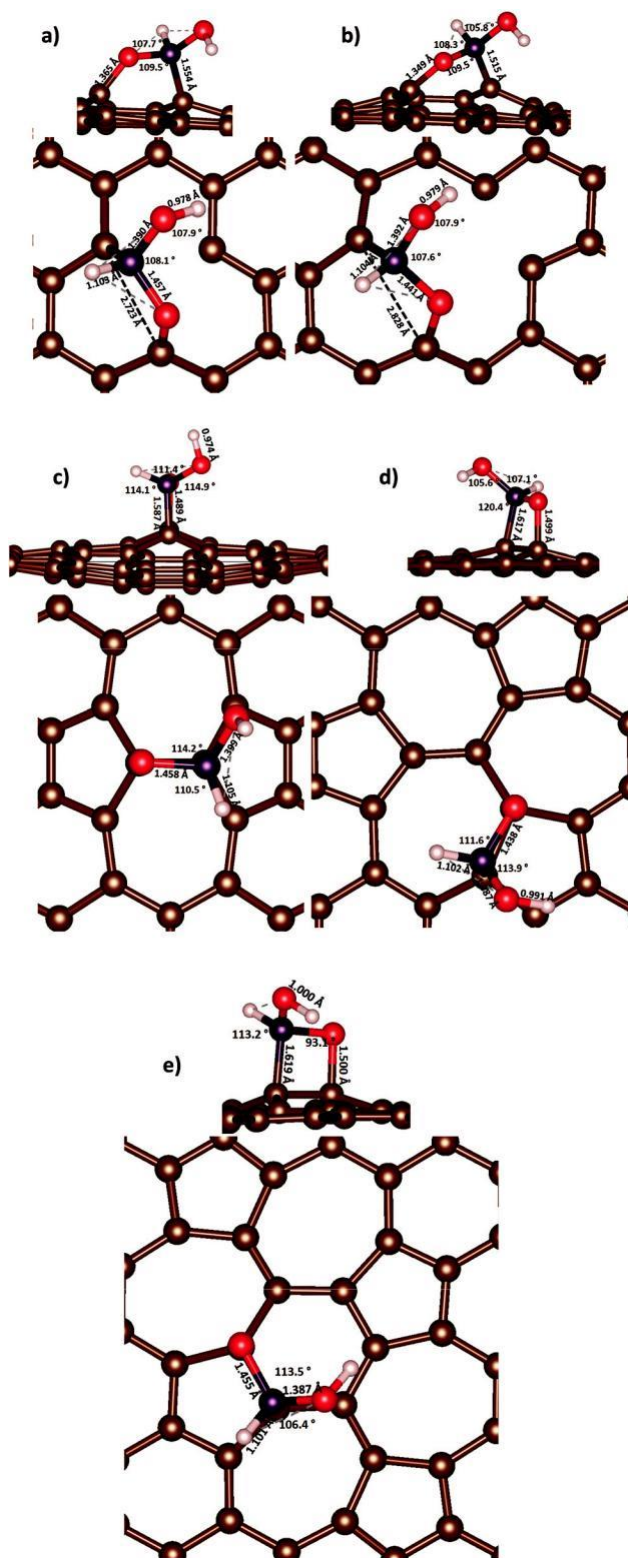

Fig. 4 Top and side views of the most favourable FA configuration on the different surfaces; (a) FA/SV, (b) FA/DV, (c) FA/SW1, (d) FA/SW2 and (e) FA/SW3. Inset shows the distances (Å) and angles (°) of interest. Carbon atoms are represented in brown, oxygen in red, hydrogen in white and the carbon atoms of formic acid in purple.

Table 3 Dissociative and molecular adsorption energies (E_{ADS}) of formic acid on the defective graphene surfaces

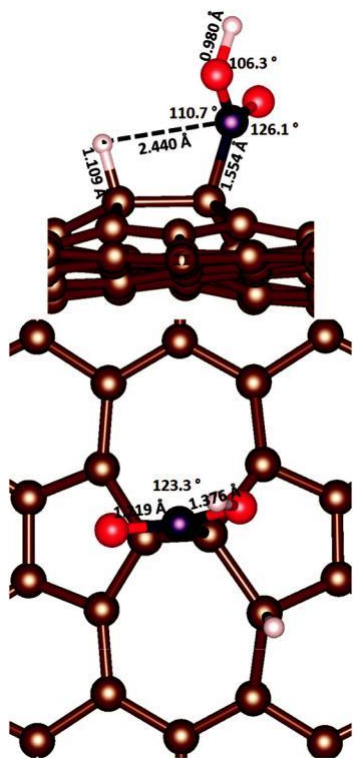| Surface	$E_{ADS\ molecular}$ (eV)	$E_{ADS\ dissociative}$ (eV)	
		(HCOO* + H*)	(COOH* + H*)
Single vacancy (SV)	−2.71	—	−3.42
Double vacancy (DV)	−1.29	—	+0.20
Stone−Wales defect (SW1)	+0.46	+0.59	−0.42
Stone−Wales defect (SW2)	+0.62	+1.19	+0.54
Stone−Wales defect (SW3)	+0.81	+0.96	+0.83

Fig. 5 Dissociative adsorption of formic acid on SW1. Carbon atoms are represented in brown, oxygen in red, hydrogen in white and the carbon atoms of formic acid in purple.

elementary step proceeds through the scission of the O−H or the C−OH bond. Both pathways showed a strong endothermic profile of +6.67 and +3.30 eV, respectively (Fig. S7 and S8†). In any case, OH and H co-adsorbed on the surface may recom-bine forming H_2O (E_R = −6.22 eV, Fig. S9†) leaving CO strongly bound to the surface (E_B = −6.71 eV), whose adsorption poisons the SV active sites.

FA may undergo the dehydrogenation pathway on the defec-tive surface, which leads to the adsorption of H, O and HCO (E_R = −1.12, Fig. S10†) through the hydroxymethylene inter-mediate, HCOH (E_R = −0.88 eV, Fig. S11†). Indeed, when FA is adsorbed on the SV site, the carbonyl C−O bond length increased to 0.22 Å compared to the gas phase structure ($d_{C−O}$ = 1.24 Å), making the breakage of the C−O bond possible. Considering the structure in Fig. S10,† it is seen that only carbon monoxide can be produced (E_R = −0.42 eV), yielding

the structure shown in Fig. S12†, where oxygen remains bound on the surface.

The recombination of adsorbed hydrogen would yield H_2 gas; however, the desorption of molecular H_2 unlikely occurs at low coverage as the desorption energy is quite endothermic (+1.85 eV). Fig. 6 shows the corresponding energy profiles of FA decomposition through the COOH and HCOH intermedi-ates on the SV structure.

Double vacancy (DV) system. Similar to SV, FA adsorption on the DV site results in an increase of the C−O bond length of 0.20 Å compared to the gas phase structure ($d_{C−O}$ = 1.24 Å). The dissociation of the C−H bond on the DV is an endother-mic process (E_R = +1.49 eV) and therefore unlikely to proceed (Fig. S13†). However, the hydroxylmethylene (Fig. S14†) inter-mediate sits only at +0.60 eV from the adsorbed HCOOH. Its dehydrogenation to HCO is strongly driven by E_R = −2.00 eV (Fig. S15†). Considering both possible decomposition path-ways, the favoured route is through the hydroxylmethylene species, followed by a highly endothermic (E_R = 4.51 eV) scis-sion of the C−H bond leading to adsorbed CO and H_2 (Fig. S16†). These species are strongly bound to the dangling bonds of the surface, thus poisoning the active sites. Fig. S17† shows the corresponding energy profiles of FA decomposition through COOH and HCOH intermediates on the DV structure.

Stone−Wales (SW1) system. The dissociative adsorption of FA on the first Stone−Wales (SW1) defect leads to a favorable co-adsorption of COOH and H (E_R = −0.42 eV, Fig. 5), while the breakage of the hydroxyl bond is endothermic (E_R = +0.59 eV) (Table 3). In this case, the reaction energy is endothermic, E_R = 5.53 eV (Fig. S18†). Following the carboxylic intermediate, we investigated the scission of the C−OH bond to CO and OH co-
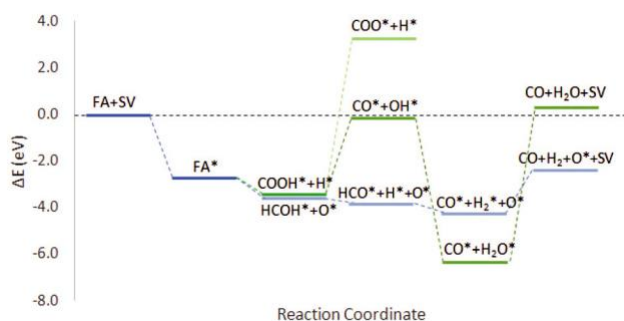

Fig. 6 Energy profile for the different pathways of formic acid decomposition on the SV structure. * indicates the adsorbed species.

adsorbed on the surface, and the breakage of the O–H bond (Fig. S19†). Both processes are highly endothermic as seen in the energy profile of Fig. S20.†

4. Conclusions

We have carried out a systematic investigation on graphitic defects as active sites using formic acid as a probe molecule. Different metal-free catalysts based on graphitic structures (pris-tine graphene, graphene oxide, PS carbon nanofibers and LHT carbon) were experimentally tested and their structures were analyzed by BET, XPS and Raman spectroscopy. We found a cor-relation between the FA conversion and the number of defects presented in the catalysts. In particular, the FA decomposition increases by increasing the defectiveness of the material, i.e. in the order GO > PR24-PS > PR24-LHT > GP. This result was con-firmed by both XPS and Raman techniques. Plotting the conver-sion vs. I_D/I_G ratio and vs. the amount of different oxygen groups displayed on the surface, we found a linear correlation between conversion and defects (R^2 = 0.99), but no direct corre-lation with oxygen groups was established. We are, then, able to ascribe the activity of the materials to the defects and not to the presence of oxygen functional groups. In order to understand the rule of the different types of defects, we investigated the decomposition of formic acid using the DFT models of pristine graphene and different defective graphene surfaces, e.g. single and double vacancies, and different Stone–Wales defects. We demonstrated that not all defects act as active centers to adsorb and decompose formic acid. The activity is mainly due to the single vacancy defect because it is the only system able to decompose formic acid to gaseous molecules, thus recycling the active site. Two different pathways were found, one passing through the carboxyl species and the other one through a hydroxymethylene intermediate. In both cases, we obtained the saturation of the active site because of CO and atomic hydrogen irreversible adsorption. For the double vacancy structure, the hydroxymethylene pathway can be compared with the one of the single vacancy defects, while for the Stone–Wales system no active sites were found able to decompose the FA molecule. Different types of oxygen functionalities (e.g. epoxide, oxygen incorporated into the structure and hydroxyl) were investigated, but they did not show any activity in the adsorption of FA, con-firming the experimental results, where no direct correlation between the oxygen groups and the catalytic behavior was observed. When the vacancies are completely saturated, the catalyst deactivates, explaining the experimental observations after 5 minutes of reaction. In conclusion, a first insight into the role of the defects present on the carbon material in FA dehydrogenation and dehydration was provided.

Conflicts of interest

There are no conflicts to declare.

References

1 K. T. Møller, T. R. Jensen, E. Akiba and H. wen Li, Prog. Nat. Sci.: Mater. Int., 2017, 27, 34–40.
2 T. N. Veziroğlu and S. Şahin, Energy Convers. Manage., 2008, 49, 1820–1831.
3 U. Sikander, S. Sufian and M. A. Salam, Int. J. Hydrogen Energy, 2017, 42, 19851–19868.
4 Z. Liu, J. Li, S. Xue, S. Zhou, K. Qu, Y. Li and W. Cai, J. Energy Chem., 2020, 47, 317–323.
5 C. Li and J. B. Baek, ACS Omega, 2020, 5, 31–40.
6 X. Zhou, Y. Huang, W. Xing, C. Liu, J. Liao and T. Lu, Chem. Commun., 2008, 3540–3542.
7 J. A. Herron, J. Scaranto, P. Ferrin, S. Li and M. Mavrikakis, ACS Catal., 2014, 4, 4434–4445.
8 Y. Cheng, X. Wu and H. Xu, Sustainable Energy Fuels, 2019, 3, 343–365.
9 B. Yin, E. Zhao, X. Hua, K. Wang, W. Wang, G. Li and T. Liu, New J. Chem., 2020, 44, 2011–2015.
10 Z. Wang, X. Hao, D. Hu, L. Li, X. Song, W. Zhang and M. Jia, Catal. Sci. Technol., 2017, 7, 2213–2220.
11 Z. Wang, H. Zhang, L. Chen, S. Miao, S. Wu, X. Hao, W. Zhang and M. Jia, J. Phys. Chem. C, 2018, 122, 12975–12983.
12 N. Gupta, O. Khavryuchenko, A. Villa and D. Su, ChemSusChem, 2017, 10, 3030–3034.
13 P. Veerakumar, P. Thanasekaran, T. Subburaj and K.-C. Lin, C, 2018, 4, 54.
14 M. M. Titirici and M. Antonietti, Chem. Soc. Rev., 2010, 39, 103–116.
15 G. Mestl, N. I. Maksimova, N. Keller, V. V. Roddatis and R. Schlögl, Angew. Chem., Int. Ed., 2001, 40, 2066–2068.
16 J. Zhang, X. Liu, R. Blume, A. Zhang, R. Schlögl and D. S. Su, Science, 2008, 322, 73–78.
17 J. Zhang, D. S. Su, R. Blume, R. Schlögl, R. Wang, X. Yang and A. Gajović, Angew. Chem., Int. Ed., 2010, 49, 8640–8644.
18 D. R. Paul, W. J. Koros, R. Y. F. Liu, Y. S. Hu, E. Baer, A. Hiltner, H. D. Keith, R. Y. F. Liu, A. Hiltner, E. Baer, R. E. Cohen, A. Bellare, R. J. Albalak, W. Hu and G. Reiter.
19 J. Xu, L. Zhang, R. Shi and Y. Zhu, J. Mater. Chem. A, 2013, 1, 14766–14772.
20 D. R. Dreyer, H. P. Jia and C. W. Bielawski, Angew. Chem., Int. Ed., 2010, 49, 6813–6816.
21 M. A. Patel, F. Luo, M. R. Khoshi, E. Rabie, Q. Zhang, C. R. Flach, R. Mendelsohn, E. Garfunkel, M. Szostak and H. He, ACS Nano, 2016, 10, 2305–2315.
22 J. H. Yang, G. Sun, Y. Gao, H. Zhao, P. Tang, J. Tan, A. H. Lu and D. Ma, Energy Environ. Sci., 2013, 6, 793–798.

23 A. Primo, F. Neatu, M. Florea, V. Parvulescu and H. Garcia, Nat. Commun., 2014, 5, 1–9.

24 Y. Gao, D. Ma, C. Wang, J. Guan and X. Bao, Chem. Commun., 2011, 47, 2432–2434.

25 H. P. Jia, D. R. Dreyer and C. W. Bielawski, Adv. Synth. Catal., 2011, 353, 528–532.

26 C. Su, M. Acik, K. Takai, J. Lu, S. J. Hao, Y. Zheng, P. Wu, Q. Bao, T. Enoki, Y. J. Chabal and K. P. Loh, Nat. Commun., 2012, 3, 1298–1299.

27 M. S. Shafeeyan, W. M. A. W. Daud, A. Houshmand and A. Arami-Niya, Appl. Surf. Sci., 2011, 257, 3936–3942.

28 M. S. Shafeeyan, W. M. A. W. Daud, A. Houshmand and A. Shamiri, J. Anal. Appl. Pyrolysis, 2010, 89, 143–151.

29 W. M. A. W. Daud and A. H. Houshamnd, J. Nat. Gas Chem., 2010, 19, 267–279.

30 H. Yu, F. Peng, J. Tan, X. Hu, H. Wang, J. Yang and W. Zheng, Angew. Chem., Int. Ed., 2011, 50, 3978–3982.

31 H. P. Jia, D. R. Dreyer and C. W. Bielawski, Tetrahedron, 2011, 67, 4431–4434.

32 J. Long, X. Xie, J. Xu, Q. Gu, L. Chen and X. Wang, ACS Catal., 2012, 2, 622–631.

33 Y. Jiang, L. Yang, T. Sun, J. Zhao, Z. Lyu, O. Zhuo, X. Wang, Q. Wu, J. Ma and Z. Hu, ACS Catal., 2015, 5, 6707–6712.

34 C. Tang, H. F. Wang, X. Chen, B. Q. Li, T. Z. Hou, B. Zhang, Q. Zhang, M. M. Titirici and F. Wei, Adv. Mater., 2016, 28, 7030.

35 L. Tao, Q. Wang, S. Dou, Z. Ma, J. Huo, S. Wang and L. Dai, Chem. Commun., 2016, 52, 2764–2767.

36 Q. Xiang, W. Yin, Y. Liu, D. Yu, X. Wang, S. Li and C. Chen, J. Mater. Chem. A, 2017, 5, 24314–24320.

37 Y. Qiu, S. Ali, G. Lan, H. Tong, J. Fan, H. Liu, B. Li, W. Han, H. Tang, H. Liu and Y. Li, Carbon, 2019, 146, 406–412.

38 Y. Gao, G. Hu, J. Zhong, Z. Shi, Y. Zhu, D. S. Su, J. Wang, X. Bao and D. Ma, Angew. Chem., Int. Ed., 2013, 52, 2109–2113.

39 Y. Jia, L. Zhang, A. Du, G. Gao, J. Chen, X. Yan, C. L. Brown and X. Yao, Adv. Mater., 2016, 28, 9532–9538.

40 S. Masuda, K. Mori, Y. Futamura and H. Yamashita, ACS Catal., 2018, 8, 2277–2285.

41 A. K. Singh, S. Singh and A. Kumar, Catal. Sci. Technol., 2016, 6, 12–40.

42 F. Joó, ChemSusChem, 2008, 1, 805–808.

43 D. J. Braden, C. A. Henao, J. Heltzel, C. C. Maravelias and J. A. Dumesic, Green Chem., 2011, 13, 1755–1765.

44 J. J. Bozell and G. R. Petersen, Green Chem., 2010, 12, 539–554.

45 F. Sanchez, M. H. Alotaibi, D. Motta, C. E. Chan-Thaw, A. Rakotomahevitra, T. Tabanelli, A. Roldan, C. Hammond, Q. He, T. Davies, A. Villa and N. Dimitratos, Sustainable Energy Fuels, 2018, 2, 2705–2716.

46 G. Kresse and J. Furthmüller, Phys. Rev. B: Condens. Matter Mater. Phys., 1996, 54, 11169–11186.

47 G. Kresse, J. Non-Cryst. Solids, 1995, 192–193, 222–229.

48 J. P. Perdew, A. Ruzsinszky, G. I. Csonka, O. A. Vydrov, G. E. Scuseria, L. A. Constantin, X. Zhou and K. Burke, Phys. Rev. Lett., 2007, 136406, 1–4.

49 N. D. Mermin, Phys. Rev., 1965, 137, A1441–A1443.

50 S. Fias, S. Van Damme and P. Bultinck, J. Comput. Chem., 2008, 29, 358–366.

51 S. Grimme, J. Antony, S. Ehrlich and H. Krieg, J. Chem. Phys., 2010, 132, 154104.

52 H. Fang, A. Roldan, C. Tian, Y. Zheng, X. Duan, K. Chen, L. Ye, S. Leoni and Y. Yuan, J. Catal., 2019, 369, 283–295.

53 X. Lu, S. Francis, D. Motta, N. Dimitratos and A. Roldan, Phys. Chem. Chem. Phys., 2020, 22, 3883–3896.

54 E. Nowicka, S. Althahban, T. D. Leah, G. Shaw, D. Morgan, C. J. Kiely, A. Roldan and G. J. Hutchings, Sci. Technol. Adv. Mater., 2019, 20, 367–378.

55 M. G. Quesne, A. Roldan, N. H. De Leeuw and C. R. A. Catlow, Phys. Chem. Chem. Phys., 2019, 21, 10750–10760.

56 R. Sundararaman and K. Schwarz, J. Chem. Phys., 2017, 146, 084111.

57 K. Mathew, R. Sundararaman, K. Letchworth-Weaver, T. A. Arias and R. G. Hennig, J. Chem. Phys., 2014, 140, 084106.

58 J. D. Pack and H. J. Monkhorst, Phys. Rev. B: Solid State, 1977, 16, 1748–1749.

59 L. P. L. Gonçalves, D. B. Christensen, M. Meledina, L. M. Salonen, D. Y. Petrovykh, E. Carbó-Argibay, J. P. S. Sousa, O. S. G. P. Soares, M. F. R. Pereira, S. Kegnæs and Y. V. Kolen'Ko, Catal. Sci. Technol., 2020, 10, 1991–1995.

60 F. Tuinstra and J. L. Koenig, J. Chem. Phys., 1970, 53, 1126–1130.

61 F. Y. Xie, W. G. Xie, L. Gong, W. H. Zhang, S. H. Chen, Q. Z. Zhang and J. Chen, Surf. Interface Anal., 2010, 42, 1514–1518.

62 G. Beamson and D. Briggs, 1992, p. Appendices 3.1 and 3.2.

63 T. Xu and L. Sun, Defects Adv. Electron. Mater. Nov. Low Dimens. Struct., 2018, 5, 137–160.

64 F. Banhart, J. Kotakoski and A. V. Krasheninnikov, ACS Nano, 2011, 5, 26–41.

65 A. V. Krasheninnikov, P. O. Lehtinen, A. S. Foster and R. M. Nieminen, Chem. Phys. Lett., 2006, 418, 132–136.

66 A. El-Barbary, H. Telling, P. Ewels, I. Heggie and R. Briddon, Phys. Rev. B: Condens. Matter Mater. Phys., 2003, 68, 1–7.

67 J. Ma, D. Alfè, A. Michaelides and E. Wang, Phys. Rev. B: Condens. Matter Mater. Phys., 2009, 80, 1–4.

68 L. Li, S. Reich and J. Robertson, Phys. Rev. B: Condens. Matter Mater. Phys., 2005, 72, 1–10.

69 D. Borisova, V. Antonov and A. Proykova, Int. J. Quantum Chem., 2013, 113, 786–791.

70 G. Do Lee, C. Z. Wang, E. Yoon, N. M. Hwang, D. Y. Kim and K. M. Ho, Phys. Rev. Lett., 2005, 95, 1–4.

71 L. Ma, J. M. Zhang, K. W. Xu and V. Ji, Appl. Surf. Sci., 2015, 343, 121–127.

72 X. Y. Liu, J. M. Zhang, K. W. Xu and V. Ji, Appl. Surf. Sci., 2014, 313, 405–410.

73 S. Yang, Z. Lan, H. Xu, G. Lei, W. Xie and Q. Gu, J. Nanotechnol., 2018, 2018, 1–5.

74 F. Solymosi, Á. Koós, N. Liliom and I. Ugrai, J. Catal., 2011, 279, 213–219.

75 X. Duan, H. Sun, Z. Ao, L. Zhou, G. Wang and S. Wang, Carbon, 2016, 107, 371–378.

76 S. Yang, G. Lei, H. Xu, B. Xu, H. Li, Z. Lan, Z. Wang and H. Gu, Appl. Surf. Sci., 2019, 480, 205–211.

77 Z. Xu, B. R. Meher, D. Eustache and Y. Wang, J. Mol. Graphics Modell., 2014, 47, 8–17.